

# $\pi$ -electron $S = \frac{1}{2}$ quantum spin-liquid state in an ionic polyaromatic hydrocarbon

Yasuhiro Takabayashi<sup>1</sup>, Melita Menelaou<sup>1,2</sup>, Hiroyuki Tamura<sup>1</sup>, Nayuta Takemori<sup>3</sup>, Takashi Koretsune<sup>3</sup>, Aleš Štefančič<sup>1,4</sup>, Gyöngyi Klupp<sup>4</sup>, A. Johan C. Buurma<sup>4</sup>, Yusuke Nomura<sup>5</sup>, Ryotaro Arita<sup>2,3</sup>, Denis Arčon<sup>6,7</sup>, Matthew J. Rosseinsky<sup>8</sup> and Kosmas Prassides<sup>1,2\*</sup>

<sup>1</sup>World Premier International–Advanced Institute for Materials Research (WPI-AIMR), Tohoku University, Sendai 980-8577, Japan, <sup>2</sup>Japan Science and Technology Agency, ERATO Isobe Degenerate  $\pi$ -Integration Project, Tohoku University, Sendai 980-8577, Japan, <sup>3</sup>RIKEN Center for Emergent Matter Science (CEMS), 2-1, Hirosawa, Wako, Saitama 351-0198, Japan, <sup>4</sup>Department of Chemistry, Durham University, Durham DH1 3LE, UK, <sup>5</sup>Department of Applied Physics, University of Tokyo, Tokyo 113-8656, Japan, <sup>6</sup>Jozef Stefan Institute, Jamova cesta 39, SI-1000 Ljubljana, Slovenia, <sup>7</sup>Faculty of Mathematics and Physics, University of Ljubljana, Jadranska cesta 19, 1000 Ljubljana, Slovenia, <sup>8</sup>Department of Chemistry, University of Liverpool, Liverpool L69 7ZD, UK.

\*e-mail: k.prassides@wpi-aimr.tohoku.ac.jp

**Molecular solids whose cooperative electronic properties are based purely on  $\pi$ -electrons from carbon atoms offer a fertile ground in the search for exotic states of matter, including unconventional superconductivity and quantum magnetism. The field was ignited by reports of high-temperature superconductivity in materials obtained by reaction of alkali metals with polyaromatic hydrocarbons (PAHs) such as phenanthrene and picene but the composition and structure of any compound in this family have remained unknown. Here, we isolate the binary caesium salts of phenanthrene,  $\text{Cs}(\text{C}_{14}\text{H}_{10})$  and  $\text{Cs}_2(\text{C}_{14}\text{H}_{10})$  to show that they are multi-orbital strongly-correlated Mott insulators. Whereas  $\text{Cs}_2(\text{C}_{14}\text{H}_{10})$  is diamagnetic due to orbital polarisation,  $\text{Cs}(\text{C}_{14}\text{H}_{10})$  is a Heisenberg antiferromagnet with a gapped spin-liquid state emerging from the highly-frustrated  $\Delta$ -chain magnetic topology of coupled alternating-exchange spiral tubes of  $S=\frac{1}{2}$   $(\text{C}_{14}\text{H}_{10})^{\bullet-}$  radical anions. The absence of long-range magnetic order down to 1.8 K ( $T/J \sim 0.02$ ,  $J$  is the dominant exchange constant) renders the compound an excellent candidate of a spin- $\frac{1}{2}$  quantum spin liquid arising purely from carbon  $\pi$ -electrons.**

Conventional Heisenberg antiferromagnets typically exhibit magnetic long-range order (AFM-LRO) below the Néel temperature,  $T_N$ . The emergence of static order can be suppressed in the presence of geometrical frustration<sup>1</sup>—the arrangement of coupled magnetic units on lattices comprising triangular or tetrahedral building blocks leads to a situation where it is impossible to simultaneously satisfy all near-neighbour exchange interactions. This results in a spin-liquid state with a highly-degenerate ground state in which strong magnetic fluctuations persist down to low temperatures. The fluctuations are further enhanced in the quantum limit of  $S=\frac{1}{2}$  spins and the resulting quantum spin liquid (QSL) prevails over AFM-LRO even at zero temperature<sup>2,3</sup>. To date the candidates for experimental realisation of QSLs remain very few. Prominent among these are the  $\text{Cu}^{2+}$  inorganic minerals, herbertsmithite ( $\text{ZnCu}_3(\text{OH})_6\text{Cl}_2$ )<sup>4</sup> and vesignieite ( $\text{BaCu}_3\text{V}_2\text{O}_8(\text{OH})_2$ )<sup>5</sup> with  $\text{Cu}^{2+}$   $S=\frac{1}{2}$  ions arranged on two-dimensional (2D) kagomé networks of corner-sharing triangular units and the

organic compounds,  $\kappa$ -(BEDT-TTF)<sub>2</sub>Cu<sub>2</sub>(CN)<sub>3</sub>, EtMe<sub>3</sub>Sb[Pd(dmit)<sub>2</sub>]<sub>2</sub> and  $\kappa$ -H<sub>3</sub>(Cat-EDT-TTF)<sub>2</sub> with a direct 2D edge-sharing triangular lattice topology<sup>6-8</sup>.

In our search for novel conducting and magnetic functionalities, we have been exploring the electronic properties of materials in which the active components of the extended structures are  $\pi$ -electron open-shell molecular units. These systems crystallise in architectures of varied dimensionality ranging from one- to three-dimensions and encompass molecular metals and superconductors such as organic charge-transfer salts<sup>9</sup> and the alkali fullerenes<sup>10-12</sup>, which provide the highest  $T_c$  (38 K)<sup>13</sup> together with molecular magnets<sup>14</sup>, including QSLs<sup>6-8</sup>, quantum spin chains and ladders<sup>15-17</sup>. In particular, interest in all-carbon  $\pi$ -electron systems was also recently revived by the report that alkali intercalation of a PAH—the five-membered-ring picene, C<sub>22</sub>H<sub>14</sub>—led to a superconductor with  $T_c$ =18 K but of unknown composition and structure<sup>18</sup>. Superconductivity was subsequently reported in alkali-intercalated phenacenes with three (phenanthrene, C<sub>14</sub>H<sub>10</sub>) and seven (1,2:8,9-dibenzopentacene, C<sub>30</sub>H<sub>18</sub>) aromatic rings ( $T_c$ =5 and 33 K, respectively)<sup>19,20</sup>. However, despite the flare of experimental and theoretical activity<sup>21-26</sup>, the results have not been reproduced and the identity of any compound in this family has remained unknown, reflecting the unavailability of phase-pure samples because of difficulties in controlling reactivity with alkali metals at high temperature<sup>18-20</sup>.

Here we isolate two members of the family of alkali intercalated PAH solids—namely, the binary salts of phenanthrene with composition Cs(C<sub>14</sub>H<sub>10</sub>) (**1**) and Cs<sub>2</sub>(C<sub>14</sub>H<sub>10</sub>) (**2**), which contain the phenanthride radical mono- and di-anion, respectively—using a solution-based route under mild conditions that avoids the competing decomposition of PAH molecules under high-temperature reaction with alkali metals. Analysis of the structural and electronic properties complemented by first-principles calculations establish both materials as two-orbital strongly-correlated Mott insulators. The di-anion salt, **2** is a low-spin,  $S=0$  system with an orbitally-polarised insulating state, which adiabatically connects to a band-insulating state. On the other hand, the  $S=1/2$  (C<sub>14</sub>H<sub>10</sub>)<sup>•-</sup> radical anions in **1** are incorporated into a magnetic network of Heisenberg antiferromagnetically-coupled spiral magnetic tubes. Coupling between neighbouring tubes *via* corner-sharing triangular units leads to a complex highly-frustrated three-dimensional (3D) spin topology of unequal-leg spin chains running along the crystallographic  $c$  axis and corner-sharing  $\Delta$ -chains<sup>27</sup> along the  $b$  direction. The magnetic behaviour of the material, which shows no magnetic order down to 1.8 K is compatible with that of a gapped QSL.

## Results and discussion

Pristine phenanthrene adopts a monoclinic structure<sup>28</sup> in which the planar molecules (Fig. 1a) form a herringbone-packing assembly of slip-stacked one-dimensional (1D) columns along the short  $b$  axis of the unit cell with interplanar angles between neighbouring molecules in adjacent chains of 58.21(7)<sup>°</sup> (Fig. 1b). Reaction of one equivalent of caesium and phenanthrene in rigorously-dried tetrahydrofuran (THF) under mild heating affords a dark olive-green crystalline material of composition Cs(C<sub>14</sub>H<sub>10</sub>). Similarly, the solvent-free dicaesium phenanthride, Cs<sub>2</sub>(C<sub>14</sub>H<sub>10</sub>) is isolated from solution as a black crystalline powder by reacting two equivalents of caesium with one equivalent of phenanthrene in dry THF under mild heating. Powder diffraction shows that both materials are of excellent crystallinity (Fig. 2a&2b) in sharp contrast to those obtained by solid state routes<sup>18-20</sup>.

The high quality of the diffraction data permitted straightforward determination of the crystal structures of both compounds. Space group assignment and extraction of unit cell dimensions

were performed by the LeBail pattern-decomposition technique. This was followed by initial structural-model generation for each system using phenanthrene units modelled as rigid bodies without internal degrees of freedom and Cs<sup>+</sup> ions. Structural model optimisation was then performed with a direct-space simulated-annealing global-optimisation technique. Refinement of the structures was finally undertaken by Rietveld analysis of the diffraction data with excellent agreement between observed and calculated profiles achieved for both systems (Fig. 2a&2b). Cs(C<sub>14</sub>H<sub>10</sub>) crystallises in the non-centrosymmetric primitive orthorhombic *P*2<sub>1</sub>2<sub>1</sub>2<sub>1</sub> space group with two crystallographically-distinct Cs<sup>+</sup> ions and two phenanthrene units in a unit cell of dimensions *a*=14.4388(2) Å, *b*=15.0250(2) Å, *c*=10.0842(1) Å at 30 K (agreement factors: *R*<sub>wp</sub>=4.80%, *R*<sub>exp</sub>=2.41%). Cs<sub>2</sub>(C<sub>14</sub>H<sub>10</sub>) is monoclinic (space group *P*2<sub>1</sub>/*a*) with one crystallographically-distinct phenanthrene unit and two Cs<sup>+</sup> ions per unit cell (lattice constants at ambient temperature: *a*=11.8129(2) Å, *b*=11.4667(2) Å, *c*=9.8269(1) Å, β=110.894(1)°; *R*<sub>wp</sub>=1.95%, *R*<sub>exp</sub>=1.98%). The fitted parameters and selected bond distances are summarized in Tables S1-S4.

The crystal structure analysis of both samples reveals that alkali intercalation and phenanthrene reduction are accompanied by drastic structural changes as the herringbone-packing motif of the pristine material is abandoned. Instead the structure of **1**, which expands by ~40 Å<sup>3</sup>/phenanthrene upon intercalation is built by triangularly-arranged trimeric units of (C<sub>14</sub>H<sub>10</sub>)<sup>•-</sup> ions (Fig. 1c). The repeat units share vertices to form spiral tubes that align along the *c* axis. The tubes (of size 11.9 Å<sup>2</sup>) adopt a bipartite packing motif in which each is surrounded by four neighbours positioned approximately at right angles (Fig. 1d). This results in the formation of zig-zag chains running parallel to the *b* axis that comprise (C<sub>14</sub>H<sub>10</sub>)<sup>•-</sup> ions from neighbouring tubes (Fig. 1e). The Cs<sup>+</sup> cations are incorporated inside the tubes and coordinate to benzene rings of adjacent phenanthrene ions with Cs<sup>+</sup>...C separations in the range of 3.119(3)-3.736(2) Å at 30 K (Table S2), implying rather strong binding of the metal ions to the phenanthrene surface. Further changes in molecular packing occur upon intercalation of the second Cs<sup>+</sup> per formula unit to afford **2**. Every other phenanthrene unit flips along the stacking direction of the pristine material in such a way as to present its benzene rings for optimal coordination by Cs<sup>+</sup> ions occupying interstitial sites above and below the molecular plane (Fig. 1f). The Cs<sup>+</sup> ions also bind to benzene rings of non-flipped adjacent (C<sub>14</sub>H<sub>10</sub>)<sup>2-</sup> units. The Cs<sup>+</sup>...C separations vary between 3.148(7) and 3.72(1) Å at room temperature (Table S4), again indicative of strong Cs<sup>+</sup>-π interactions. The resulting expanded structure (by ~66 Å<sup>3</sup>/phenanthrene) is that of an assembly of zig-zag chains of (C<sub>14</sub>H<sub>10</sub>)<sup>2-</sup> units alternately tilted by 72.3(6)°. The Raman and infrared (IR) spectra of **1** and **2** show softening and broadening of the vibrational modes upon reduction, consistent with the antibonding nature of the LUMO and theoretically-predicted<sup>29</sup> strong electron-phonon coupling, respectively (Fig. 2c&S1). Although softening is mostly monotonic, it is rarely linear with increasing charge (Table S5), unlike C<sub>60</sub>, where the A<sub>g</sub>(2) mode downshifts quasi-linearly (~6 cm<sup>-1</sup>/charge)<sup>30,31</sup>.

Magnetisation data from both compounds (Fig. 3a) do not show evidence for either metallic behaviour or superconductivity. The molar magnetic susceptibility, χ(*T*) of **1** displays a broad maximum at ~40 K together with a sharp upturn at low *T* due to impurity-spin contributions. There is no deviation between zero-field-cooled (ZFC) and field-cooled (FC) measurements. Above 100 K, χ(*T*) follows the Curie-Weiss law yielding an effective moment, μ<sub>eff</sub>=1.76(1) μ<sub>B</sub>/C<sub>14</sub>H<sub>10</sub> (consistent with *S*=½/phenanthrene) and a Weiss temperature, Θ=-72.5(1) K indicative of strong AFM exchange interactions. χ(*T*) of **2** is drastically different and consistent with the presence of a low-spin diamagnetic (C<sub>14</sub>H<sub>10</sub>)<sup>2-</sup> anion.

A more definitive characterisation of the magnetic properties is achieved by electron paramagnetic resonance (EPR) spectroscopy, which directly measures spin susceptibilities of individual components. At ambient temperature, the X-band EPR spectrum of **1** comprises two components (Fig. 3b): a majority nearly-ideal Lorentzian line at  $g=2.0007(3)$  with width,  $\Delta B=15.29(1)$  mT and a barely-discernible minority  $g$ -factor-broadened one. The proximity of  $g$  to the free-electron value,  $g_e=2.0023$  signifies the presence of electronically-active  $(C_{14}H_{10})^{\bullet-}$  radical anions and nearly-complete electron transfer from Cs to  $C_{14}H_{10}$ . Neither component shows Dysonian lineshape asymmetry, characteristic of a metallic state. We conclude that **1** is an insulator. The intensity of the minority component (~5% of all spins) follows a Curie-like temperature dependence (Fig. 3c) and is ascribed to impurity or defect states. A similar low-intensity Curie-like line characterises the EPR spectrum of diamagnetic **2**, which is thus also insulating (Fig. S2). The non-Fano lineshape of the IR peaks (Fig. 2c) is consistent with the insulating state assignment of **1** and **2**. On the other hand, the intensity of the main broad component in the EPR spectrum of **1** mimics the temperature response of the SQUID magnetic susceptibility. It first increases on cooling, reaches a broad maximum at ~42 K, and then starts to decrease approaching zero as  $T \rightarrow 0$  K (Fig. 3c), thereby implying the presence of some spin-gap in the excitation spectrum. The low-temperature suppression of the main EPR line is not accompanied by the emergence of an antiferromagnetic resonance characteristic of a transition to a long-range ordered antiferromagnetic (LRO-AFM) state.

The magnetic data of **1**—a broad  $\chi(T)$  maximum at  $T_{\max}$  and the emergence of a spin-gap at lower temperatures—are reminiscent of the response of  $S=1/2$  antiferromagnetic alternating-exchange Heisenberg spin chains<sup>32</sup>. Indeed good agreement with the combined EPR and SQUID spin-susceptibility data over the entire temperature range is found for this model—the global fit (Fig. 3c) yields an intrachain exchange constant,  $J/k_B=77.9(3)$  K, an alternation parameter,  $\alpha=0.687(5)$  and a Curie constant,  $C=0.301(1)$  emu K mol<sup>-1</sup> (consistent with  $S=1/2$ /phenanthrene). However, despite the excellent fit of the purely 1D magnetic model to the experimental data, the existence of interchain magnetic coupling is immediately evident in the temperature evolution of the EPR linewidth,  $\Delta B$ . The gradual increase in  $\Delta B$  at low temperatures (Fig. S3) cannot be rationalised solely within 1D models<sup>33</sup>. It implies the growth of spin correlations and necessitates finite interchain magnetic exchange<sup>34</sup>. This in turn is known to stabilise LRO-AFM for both disorder-free and disordered systems<sup>35</sup>. Then, the experimentally-observed robustness of the quantum spin state and absence of LRO-AFM in **1** to temperatures as low as  $T \approx 0.02J$  imply that the simplified  $J$ - $\alpha J$  alternating-spin-chain model needs to be replaced by a more realistic alternative.

First-principles electronic structure calculations of **1** and **2** within the generalized-gradient approximation (GGA) based on density functional theory (DFT) reveal that the bands originating from the LUMO and LUMO+1 orbitals are heavily entangled in both systems (Fig. 4a&b). The low-energy bands around the Fermi level are made of both molecular orbitals with energy splittings much smaller than the bandwidth ( $W \sim 0.5$  eV). Therefore upon electron doping, the added electrons partially populate both bands so that  $Cs(C_{14}H_{10})$  and  $Cs_2(C_{14}H_{10})$  are two-orbital systems with a  $1/4$ - and  $1/2$ -filled band, respectively. Both systems are thus expected to be metals—this is in striking contrast with experiment, which shows that they are insulators. The absence of metallic behaviour provides the signature of the importance of strong correlations. Properly-correlated first-principles calculations of the on-molecule electron repulsion energy,  $U$  for phenanthrene pairs in the  $Cs(C_{14}H_{10})$  crystal find values ranging between 1.1 and 1.8 eV (Fig. S4&Table S6). As the bands in which the electrons move are narrow due to the weak intermolecular overlap,  $(U/W)$  is on the order of 2-3

implying that the large on-site Coulomb repulsion could overcome the kinetic energy favouring electron delocalisation (quantified by  $W$ ) and lead to Mott insulating ground states for both integer,  $n=1,2$  doping levels, as observed experimentally. Hund's rule coupling,  $J_H$  promotes insulating behaviour at half-filling but diminishes the effect of correlations and leads to a reduced Mott gap in the singly-occupied case<sup>36</sup>. However,  $J_H$  is very small in multi-orbital strongly correlated molecular solids (the net Hund's coupling can be even smaller because of the presence of phonon contributions favouring low-spin configuration)<sup>37,38</sup> and therefore unable to sustain metallicity in the  $n=1$  Cs(C<sub>14</sub>H<sub>10</sub>) system. Dynamical mean-field theory (DMFT) calculations<sup>39</sup> of two-orbital correlated systems at half filling also reveal the existence of two fundamentally different Mott phases, a high-spin ( $S=1$ ) one characterized by vanishing orbital susceptibility and a low-spin ( $S=0$ ) one adiabatically connected to the band insulating state (that is, an orbitally-polarised Mott insulating state). Materials in which  $J_H$  is very small and dominated by the level splitting<sup>37</sup> are found to lie in the orbitally-polarised Mott insulator part of the phase diagram<sup>39</sup>, naturally accounting for the experimentally-observed diamagnetism in Cs<sub>2</sub>(C<sub>14</sub>H<sub>10</sub>). The effect of electron correlation in the two near-degenerate bands of Cs<sub>2</sub>(C<sub>14</sub>H<sub>10</sub>) was confirmed explicitly by performing DFT+DMFT calculations, which establish that correlations enhance orbital polarisation and push the system towards the orbitally-polarised low-spin ( $S=0$ ) Mott state (Fig. S5a&b) in agreement with experiment.

The intermolecular spin interactions in **1** were evaluated by assuming an effective Heisenberg model and performing first-principles calculations on phenanthride pairs within an intermolecular centre-to-centre distance of 8.0 Å (Table S6) considering the spin-density distribution and molecular orbital overlap. The LUMO wavefunctions whose population on Cs is very small (Cs charge = +0.9), in agreement with the EPR experiments, are distributed over molecular pairs and exhibit biradical character, consistent with electronic localisation (Fig. S6). We found that the dominant direct antiferromagnetic interactions are between pairs of crystallographically-independent (C<sub>14</sub>H<sub>10</sub>)<sub>A</sub><sup>•-</sup> and (C<sub>14</sub>H<sub>10</sub>)<sub>B</sub><sup>•-</sup> units, which comprise the building components of the tubular assemblies running along the  $c$  axis (Fig. 1c). There are two distinct couplings with exchange constants,  $J=49$  K and  $\alpha J=44$  K leading to the formation of spiral magnetic tubes aligning parallel to  $c$  and comprising antiferromagnetically-coupled alternating-exchange spin- $\frac{1}{2}$  molecular units (Fig. 5a). The second set of leading exchange interactions,  $J_{\text{inter}}=30$  K and  $J'_{\text{inter}}=28$  K, which emerges from the calculations, corresponds to coupling between neighbouring tubes (Fig. 1e). These define a set of magnetic  $\Delta$ -chains—chains of corner-sharing triangular units, a fully-frustrated quantum spin system<sup>27</sup>—running parallel to the  $b$  axis (Fig. 5b&S7). The resulting 3D interlinked staircase-like spin topology is illustrated in Fig. 5c&S8.

The salient features of the microscopic magnetic model (Fig. 5c), which emerge from the first-principles calculations can be summarized as follows: (a) the dominant exchange coupling,  $J$  occurs within the  $c$ -axis tubes, (b) there is a small bond alternation ( $\alpha\sim 0.9$ ), (c) interchain couplings,  $J_{\text{inter}}$  and  $J'_{\text{inter}}$  are not small ( $\gamma=\langle J_{\text{inter}} \rangle / \langle J \rangle \sim 0.6$ ), and (d) due to interchain coupling, the system is highly frustrated. Since  $J$  is the largest exchange constant, we first investigated whether the experimental  $\chi(T)$  data can be reproduced by employing a model of coupled unequal-leg Heisenberg chains where frustration in the interchain coupling has not been included. Quantum Monte Carlo (QMC) calculations were performed for three models in which a fixed sum of exchange constants was retained: (i) decoupled ( $\gamma=0$ ) alternating chains with an alternation parameter,  $\alpha=0.7$ , (ii) coupled ( $\gamma=0.3$ ) alternating chains with an alternation parameter,  $\alpha=0.4$ , and (iii) 3D uniformly-coupled alternating chains with  $\alpha=0.6$  and four interchain exchange interactions in the  $ab$  plane with  $\gamma=0.025$ . We find that the calculated uniform susceptibility (Fig. S9a) is in good agreement with experiment in

all cases. However, the absence of AFM-LRO in the experiment can be only reproduced by the QMC calculations when we assume that the bond alternation is strong enough or the interchain exchange coupling is extremely small (Fig. S9b). These results necessitate that the interchain frustration, which is not considered in the present QMC calculation, is crucially important for stabilising the spin-liquid state. The vanishing of the spin susceptibility below 6 K ( $\sim 0.1 J/k_B$ ) implies that the spins of the  $(C_{14}H_{10})^{\bullet-}$  radical ions form a collective spin-singlet ground state compatible with a 3D QSL whose spin excitation spectrum has a finite gap. The magnitude of the gap opening for the spinon excitations can be extracted as  $\Delta \sim 30$  K by fitting the low-temperature spin-susceptibility data to an exponential function,  $\chi(T) \propto \exp(-\Delta/T)$  (Fig. 3c(inset)&S10).

The combined experimental and theoretical data described here have allowed us to track the evolution of the structures and electronic states of ionic salts of phenanthrene with change in molecular oxidation state. Because the herringbone structure of pristine PAHs does not contain well-defined interstitial space to accommodate the alkali intercalants, intercalation is enabled only if new molecular packing motifs are adopted. Here non-herringbone-packed structures were accessed for both  $Cs(C_{14}H_{10})$  and  $Cs_2(C_{14}H_{10})$  compositions *via* solvent dissolution and reprecipitation of the phenanthrene host in the presence of reducing agents without the commonly-encountered metal-bound solvent incorporation<sup>40,41</sup>. A complementary approach to structural engineering is offered by redox-controlled solid state routes—these are shown to afford  $K_2(C_{22}H_{14})$  salts ( $C_{22}H_{14}$ =picene, pentacene) with potassium intercalation enabled by cooperative molecular reorientations, which expand the herringbone packing and create new crystallographic interstices for the cations to occupy (accompanying paper)<sup>42</sup>.

Turning to the electronic properties, both  $Cs(C_{14}H_{10})$  and  $Cs_2(C_{14}H_{10})$  display correlated-electron Mott localisation. Although orbital degeneracy is impossible because the symmetry of the phenanthrene molecule is too low, the LUMO and LUMO+1 levels are accidentally near-degenerate and heavily entangled in the solid state—this renders **1** and **2** two-orbital systems with formal  $1/4$ - and  $1/2$ -bandfilling in the absence of correlations (Fig. 4) and raises interesting questions as to the origin of the filling-dependent electronic behaviour. For singly-occupied shells, metallicity strongly competes with the insulating state as the Mott gap is suppressed by Hund’s rule coupling,  $J_H$ <sup>36</sup>. This pertains to *d*-electron transition metal compounds but its relevance is significantly diminished in *p*-electron molecular systems, such as  $Cs(C_{14}H_{10})$  due to the small intramolecular  $J_H$  values<sup>37,38</sup> and the Mott state survives. For half-filled shells,  $U$  and  $J_H$  work synergetically and the stability of the Mott state in  $Cs_2(C_{14}H_{10})$  is enhanced. On the other hand, the “low-spin”  $S=0$  state shows the dominant energy for the two electrons localized on the  $(C_{14}H_{10})^{2-}$  anion by  $U$ ; DFT+DMFT calculations show that the crystal field splitting overcomes the intramolecular Hund’s rule electron repulsion to stabilize one of the two quasi-degenerate entangled orbitals, which is preferentially occupied by two electrons. This results in an orbitally-polarised low-spin Mott insulator, which is adiabatically connected to a band-insulating state<sup>39</sup>. Such a state is rare among transition metal compounds but should be ubiquitous in correlated molecular solids at even numbers of doped carriers. Its current scarcity is presumably related to the experimental difficulty of distinguishing it from a band insulator—a label routinely used to describe diamagnetic insulating solids.

To date, quantum-spin-liquid behaviour has been rare and its possible emergence in frustrated systems is dominated by antiferromagnetically-coupled spin- $1/2$   $Cu^{2+}$  *d*<sup>9</sup>-ions adopting kagomé magnetic topologies<sup>4,5</sup> and by 2D edge-sharing triangularly-arranged spin- $1/2$  molecular pairs in organic charge-transfer salts close to the Mott boundary<sup>6-8</sup>. More recent examples include arrangements based on *d*<sup>1</sup> ions—Kagomé networks of  $V^{4+}$  in an oxyfluoride<sup>43</sup> and of  $Cr^{5+}$  in  $Ca_{10}Cr_7O_{28}$

with a complex frustration mechanism involving both ferromagnetic and antiferromagnetic couplings<sup>44</sup>. Therefore **1** emerges as a rare example of a spin- $\frac{1}{2}$  molecular quantum antiferromagnet with a frustrated 3D-interlinked exchange network based uniquely on carbon  $p\pi$ -electron states. Experiment here shows the absence of a transition to an ordered state even at temperatures much lower than the scale defined by the strength of magnetic interactions,  $J/k_B$  and consistent with a large frustration parameter,  $f=J/T_N$  (lower limit,  $f\sim 50$ ). At the same time, the spin susceptibility approaches zero exponentially at low temperatures implying that the ground state has a zero spin and is separated from the first excited state by an energy gap. The electronic behaviour of **1** is therefore compatible with that of a 3D gapped QSL ground state as supported by the evaluated topology and strength of several different isotropic exchange couplings.

## Conclusions

In summary, we have shown that by using mild conditions (this work) and controlling the power of the reducing agents (accompanying paper)<sup>42</sup>, it is possible to access novel crystalline metal PAH solids with a diverse variety of molecular packing motifs and of varying molecular oxidation state, while retaining the close intermolecular contact required for functional electronic response. Both phenanthrene compounds, **1** and **2** present examples of multi-orbital strongly-correlated Mott insulators, a rare phenomenon in molecular electronic materials beyond high-symmetry fullerenes<sup>10-13</sup>. In addition, **1** exhibits a completely new frustrated magnetic topology thereby emerging as an excellent candidate for realizing the long-sought  $S=\frac{1}{2}$  quantum spin-liquid ground state<sup>3</sup>, here arising purely from carbon  $\pi$ -electrons.

## Methods

**Abbreviations.** BEDT-TTF: bis(ethylenedithio)-tetrathiafulvalene; dmit: 1,3-dithiole-2-thione-4,5-dithiolate; Cat: catechol; Et: ethyl; Me: methyl.

**Synthesis of Cs(C<sub>14</sub>H<sub>10</sub>) (**1**) and Cs<sub>2</sub>(C<sub>14</sub>H<sub>10</sub>) (**2**).** Both compounds were synthesized by reaction of Cs metal with phenanthrene in THF solution. Elemental analysis—calculated (%) for C<sub>14</sub>H<sub>10</sub>Cs: C 54.04, H 3.24; found C 54.12, H 3.28; calculated (%) for C<sub>14</sub>H<sub>10</sub>Cs<sub>2</sub>: C 37.87, H 2.27; found C 37.36, H 2.30.

**Structural analysis.** Synchrotron X-ray powder diffraction data for **1** were collected between 30 and 300 K with the high-resolution multi-detector diffractometer on beamline ID22 ( $\lambda=0.35420$  Å) at the ESRF, Grenoble. Laboratory data for **2** were collected at ambient temperature with a Rigaku SmartLab ( $\lambda=1.54056$  Å) diffractometer operating in transmission mode. Preliminary analysis of the diffraction data was performed with the EXPO2014 suite of programs<sup>45</sup> using direct-space simulated-annealing approaches with the phenanthrene moieties treated as rigid bodies followed by final Rietveld refinements with the GSAS suite<sup>46</sup>.

**Vibrational spectroscopy.** IR measurements were performed on KBr pellets with a Bruker Alpha spectrometer (resolution,  $2\text{ cm}^{-1}$ ) inside an Ar-filled glovebox. Raman spectra were collected in backscattering geometry with a Horiba Jobin Yvon LabRAM HR spectrometer with a 633 nm (at 0.37 mW power) or a 532 nm (at 0.09 mW power) laser focused to a spot of  $\sim 1\ \mu\text{m}$  in diameter on samples sealed in glass capillaries. Higher laser power led to irreversible changes.

**Magnetic measurements.** These were performed on samples (**1**, 31.7 mg; **2**, 31.5 mg) sealed in thin-walled quartz ampoules under a helium partial pressure ( $\sim 300$  mbar) with a Quantum Design SQUID MPMS magnetometer. Magnetic susceptibility,  $\chi(T)$  data were collected at fields between 0.005 and 1 T (**1**) and at 5 T (**2**) under FC and at 0.005 and 0.01 T (**1**) under ZFC between 1.8 and 300 K.

Magnetisation,  $M(H)$  measurements at ambient temperature confirmed the absence of adventitious ferromagnetic impurities in both materials. Corrections for the diamagnetic core contribution of  $\text{Cs}^+$  and phenanthrene ( $-0.35 \times 10^{-4}$  and  $-1.2086 \times 10^{-4}$  emu mol $^{-1}$ , respectively) were applied.  $\chi(T)$  of **1** was fitted together with the EPR spin susceptibility, as described below.  $\chi(T)$  of **2** was fitted to the Curie-Weiss law,  $\chi = \chi_0 + C/(T - \Theta)$ , where  $\chi_0$  is a temperature-independent term,  $C$  is the Curie constant, and  $\Theta$  is the Weiss temperature.

**EPR spectroscopy.** X-band ( $\sim 9.6$  GHz) EPR experiments were performed on cooling on samples of **1** and **2** sealed under dynamic vacuum in Suprasil quartz tubes with a home-built spectrometer equipped with a Varian E-101 microwave bridge and TEM104 dual-cavity resonator and an Oxford Instruments ESR900 cryostat with ITC503 temperature controller (stability,  $\pm 0.05$  K). The microwave power was 1 mW. The EPR and SQUID  $\chi(T)$  data of **1** were fitted to the expression for the magnetic susceptibility of a spin- $\frac{1}{2}$  antiferromagnetic alternating-exchange Heisenberg chain, described by the Hamiltonian,  $H = \sum_i (J S_{2i-1} S_{2i} + \alpha J S_{2i} S_{2i+1})$ , where  $J$  is the intrachain exchange constant and  $0 < \alpha < 1$  an alternation parameter<sup>32</sup>. The SQUID data were corrected for a Curie-like defect contribution to the susceptibility by subtracting the spin susceptibility of the narrow EPR component.

**DFT calculations.** First-principles calculations were performed within the generalized-gradient approximations (GGA)<sup>47</sup> based on DFT with the QUANTUM-ESPRESSO package<sup>48</sup>. Ultrasoft pseudopotentials<sup>49</sup> and plane wave basis sets with cutoff energies of 46 Ry for wave functions and 318 Ry for charge densities were used. A  $3 \times 3 \times 4$  and a  $4 \times 4 \times 5$   $k$ -mesh were employed for **1** and **2**, respectively. The maximally-localized Wannier functions for the low-energy bands around the Fermi level were then constructed with the Wannier90 code<sup>50</sup>.

**DFT+DMFT calculations.** The effect of electron correlation on the LUMO and LUMO+1 orbitals in **2** was studied by DFT+DMFT calculations. The local (intramolecular) self-energy was calculated for each molecule in the unit cell. In practice, the calculation can be done for a single molecule exploiting the fact that the four phenanthrene units are equivalent by symmetry. We solved the two-orbital impurity problem at the temperature of 100 K by the continuous-time quantum Monte Carlo method<sup>51</sup>. The intraorbital Hubbard interaction  $U$  was set to be 1 eV. The interorbital interaction  $U'$  is given by  $U' = U - 2J_{\text{eff}}$  where  $J_{\text{eff}}$  is the effective local exchange interaction. The double counting correction,  $\Delta\epsilon$  at the Hartree level is subtracted from the onsite levels of LUMO and LUMO+1 orbitals;  $\Delta\epsilon$  is given by  $U N_{\text{LUMO}} + U' N_{\text{LUMO}+1}$  and  $U N_{\text{LUMO}+1} + U' N_{\text{LUMO}}$  for the LUMO and LUMO+1 orbitals, respectively ( $N$  = orbital occupation at the DFT level). The small orbital off-diagonal self-energy was neglected in the DMFT simulation.

**Quantum-chemical calculations.** Spin-flip and on-site electron repulsion,  $U$  energies were calculated by properly-correlated first-principles calculations using multi-reference second-order perturbation theory (MRMP2) with complete active space self-consistent field (CASSCF) optimized orbitals where the active space consists of singly-occupied LUMOs of two molecules (MRMP2(2,2) method) (Fig. S6). We employed the double-zeta valence basis set with the SBKJC pseudopotential, in which ( $p, d$ ) polarisation and ( $s, p$ ) diffuse functions are added for the phenanthrene units.

**QMC calculations.** The magnetic susceptibility was evaluated by applying the loop cluster algorithm implemented in the code LOOP in the ALPS libraries<sup>52</sup> on 16,000 sites ( $20 \times 20 \times 40$ ). Statistical errors were confirmed to be low enough in the plot by using 5000 thermalisation steps and 10,000 sweeps after thermalisation.

## References



1. Ramirez, A. P. Strongly geometrically frustrated magnets. *Annu. Rev. Mater. Sci.* **24**, 453–480 (1994).
2. Balents, L. Spin liquids in frustrated magnets. *Nature* **464**, 199–208 (2010).
3. Imai, T. & Lee, Y. S. Do quantum spin liquids exist? *Phys. Today* **69**, 30–36 (2016).
4. Fu, M., Imai, T., Han, T.-H. & Lee, Y. S. Evidence for a gapped spin-liquid ground state in a kagome Heisenberg antiferromagnet. *Science* **350**, 655–658 (2015).
5. Okamoto, Y., Yoshida, H. & Hiroi, Z. Vesignieite  $\text{BaCu}_3\text{V}_2\text{O}_8(\text{OH})_2$  as a candidate spin- $\frac{1}{2}$  kagomé antiferromagnet. *J. Phys. Soc. Jpn* **78**, 033701 (2009).
6. Shimizu, Y., Miyagawa, K., Kanoda, K., Maesato, M. & Saito, G. Spin liquid state in an organic Mott insulator with a triangular lattice. *Phys. Rev. Lett.* **91**, 107001 (2003).
7. Ito, T., Oyamada, A., Maegawa, S., Tamura, M. & Kato, R. Spin-liquid state in an organic spin- $\frac{1}{2}$  system on a triangular lattice,  $\text{EtMe}_3\text{Sb}[\text{Pd}(\text{dmit})_2]_2$ . *J. Phys.: Condens. Matter* **19**, 145247 (2007).
8. Isono, T. *et al.* Gapless quantum spin liquid in an organic spin-1/2 triangular-lattice  $\kappa\text{-H}_3(\text{Cat-EDT-TTF})_2$ . *Phys. Rev. Lett.* **112**, 177201 (2014).
9. Saito, G. & Yoshida, Y. Development of conductive organic molecular assemblies: organic metals, superconductors, and exotic functional materials. *Bull. Chem. Soc. Jpn* **80**, 1–137 (2007).
10. Takabayashi, Y. *et al.* The disorder-free non-BCS superconductor  $\text{Cs}_3\text{C}_{60}$  emerges from an antiferromagnetic insulator parent state. *Science* **323**, 1585–1590 (2009).
11. Ganin, A. Y. *et al.* Polymorphism control of superconductivity and magnetism in  $\text{Cs}_3\text{C}_{60}$  close to the Mott transition. *Nature* **466**, 221–225 (2010).
12. Zadik, R. H. *et al.* Optimized unconventional superconductivity in a molecular Jahn-Teller metal. *Sci. Adv.* **1**, e1500059 (2015).
13. Ganin, A. Y. *et al.* Bulk superconductivity at 38 K in a molecular system. *Nature Mater.* **7**, 367–371 (2008).
14. Veciana, J. (Ed.)  *$\pi$ -Electron magnetism. From molecules to magnetic materials* (Springer, Berlin Heidelberg, 2001).
15. Yamaguchi, H. *et al.*, Unconventional magnetic and thermodynamic properties of  $S = 1/2$  spin ladder with ferromagnetic legs. *Phys. Rev. Lett.* **110**, 157205 (2013).
16. Riyadi, S. *et al.* Antiferromagnetic  $S = \frac{1}{2}$  spin chain driven by  $p$ -orbital ordering in  $\text{CsO}_2$ . *Phys. Rev. Lett.* **108**, 217206 (2012).
17. Klanjšek, M. *et al.* Phonon-modulated magnetic interactions and spin Tomonaga-Luttinger liquid in the  $p$ -orbital antiferromagnet  $\text{CsO}_2$ . *Phys. Rev. Lett.* **115**, 057205 (2015).
18. Mitsuhashi, R. *et al.* Superconductivity in alkali-metal-doped picene. *Nature* **464**, 76–79 (2010).
19. Wang, X. F. *et al.* Superconductivity at 5 K in alkali-metal-doped phenanthrene. *Nature Commun.* **2**, 507 (2011).
20. Xue, M. *et al.* Superconductivity above 30 K in alkali-metal-doped hydrocarbon. *Sci. Rep.* **2**, 389 (2012).
21. Kosugi, T. *et al.* First-principles electronic structure of solid picene. *J. Phys. Soc. Jpn* **78**, 113704 (2009).
22. de Andres, P. L., Guijarro, A. & Vergés, J. A. *Ab initio* electronic and geometrical structures of tripotassium-intercalated phenanthrene. *Phys. Rev. B* **84**, 144501 (2011).
23. Mahns, B., Roth, F. & Knupfer, M. Absence of photoemission from the Fermi level in potassium intercalated picene and coronene films: Structure, polaron, or correlation physics? *J. Chem. Phys.* **136**, 134503 (2012).

24. Ruff, A. *et al.* Absence of metallicity in K-doped picene: Importance of electronic correlations. *Phys. Rev. Lett.* **110**, 216403 (2013).
25. Naghavi S. S. & Tosatti, E. Crystal structure search and electronic properties of alkali-doped phenanthrene and picene. *Phys. Rev. B* **90**, 075143 (2014).
26. Heguri, S., Kobayashi, M. & Tanigaki, K. Questioning the existence of superconducting potassium doped phases for aromatic hydrocarbons. *Phys. Rev. B* **92**, 014502 (2015).
27. Kubo, K. Excited states and the thermodynamics of a fully frustrated quantum spin chain. *Phys. Rev. B* **48**, 10552–10555 (1993).
28. Kay, M. I., Okaya, Y. & Cox, D. E. A refinement of the structure of the room temperature phase of phenanthrene, C<sub>14</sub>H<sub>10</sub>, from X-ray and neutron diffraction data. *Acta Cryst. B* **27**, 26–33 (1971).
29. Kato, T., Yoshizawa, K. & Hirao, K. Electron–phonon coupling in negatively charged acene- and phenanthrene-edge-type hydrocarbon crystals. *J. Chem. Phys.* **116**, 3420–3429 (2002).
30. Kuzmany, H., Matus, M., Burger, B. & Winter, J. Raman scattering in C<sub>60</sub> fullerenes and fullerides. *Adv. Mater.* **6**, 731–745 (1994).
31. Kosaka, M. *et al.* Superconductivity in Li<sub>x</sub>CsC<sub>60</sub> fullerides. *Phys. Rev. B* **59**, R6628–R6630 (1999).
32. Johnston, D. C. *et al.* Thermodynamics of spin  $S = \frac{1}{2}$  antiferromagnetic uniform and alternating-exchange Heisenberg chains. *Phys. Rev. B* **61**, 9558–9606 (2000).
33. Oshikawa, M. & Affleck, I. Low-temperature electron spin resonance theory for half-integer spin antiferromagnetic chains. *Phys. Rev. Lett.* **82**, 5136–5139 (1999).
34. Furuya, S. C. & Sato, M. Electron spin resonance in quasi-one-dimensional quantum antiferromagnets: Relevance of weak interchain interactions. *J. Phys. Soc. Jpn* **84**, 033704 (2015).
35. Lemmens, P., Güntherodt, G. & Gros, C. Magnetic light scattering in low-dimensional quantum spin systems. *Phys. Rep.* **375**, 1–103 (2003).
36. de’ Medici, L., Mravlje, J. & Georges, A. Janus-faced influence of Hund’s rule coupling in strongly correlated materials. *Phys. Rev. Lett.* **107**, 256401 (2011).
37. Nomura, Y., Nakamura, K. & Arita, R. *Ab initio* derivation of electronic low-energy models for C<sub>60</sub> and aromatic compounds. *Phys. Rev. B* **85**, 155452 (2012).
38. Nomura, Y. *et al.* Unified understanding of superconductivity and Mott transition in alkali-doped fullerides from first principles. *Sci. Adv.* **1**, e1500568 (2015).
39. Werner, P. & Millis, A. J. High-spin to low-spin and orbital polarization transitions in multiorbital Mott systems. *Phys. Rev. Lett.* **99**, 126405 (2007).
40. Smith, J. D. Organometallic compounds of the heavier alkali metals. *Adv. Organomet. Chem.* **43**, 267–348 (1999).
41. Zabula, A. V. & Petrukhina, M. A. Structural perspective on aggregation of alkali metal ions with charged planar and curved carbon  $\pi$ -surfaces. *Adv. Organomet. Chem.* **61**, 375–462 (2013).
42. Romero, F. D. *et al.* Redox-controlled potassium intercalation into two polyaromatic hydrocarbon solids: creating cation sites by molecular reorientation (accompanying paper).
43. Aidoudi, F. H. *et al.* An ionothermally prepared  $S = \frac{1}{2}$  vanadium oxyfluoride kagome lattice. *Nature Chem.* **3**, 801–806 (2011).
44. Balz, C. *et al.* Physical realization of a quantum spin liquid based on a complex frustration mechanism. *Nature Phys.* **12**, 942–949 (2016).
45. Altomare, A. *et al.* EXPO2013: a kit of tools for phasing crystal structures from powder data. *J. Appl. Crystallogr.* **46**, 1231–1235 (2013).
46. Larson, A. C. & von Dreele, R. B. *GSAS software* (Los Alamos National Laboratory Report No. LAUR 86-748, 2000).

47. Perdew, J. P.; Burke, K. & Ernzerhof, M. Generalized gradient approximation made simple. *Phys. Rev. Lett.* **77**, 3865–3868 (1996).
48. Giannozzi, P. *et al.* QUANTUM ESPRESSO: a modular and open-source software project for quantum simulations of materials. *J. Phys.: Condens. Matter* **21**, 395502 (2009).
49. Vanderbilt, D. Soft self-consistent pseudopotentials in a generalized eigenvalue formalism. *Phys. Rev. B* **41**, 7892(R)–7895(R) (1990).
50. Mostofi, A. A. *et al.* Wannier90: a tool for obtaining maximally-localised Wannier functions. *Comput. Phys. Commun.* **178**, 685–699 (2008).
51. Nomura, Y., Sakai, S. & Arita, R. Multiorbital cluster dynamical mean-field theory with an improved continuous-time quantum Monte Carlo algorithm. *Phys. Rev. B* **89**, 195146 (2014).
52. Bauer, B. *et al.* The ALPS project release 2.0: open source software for strongly correlated systems. *J. Stat. Mech. Theor. Exp.* P05001 (2011).

### Acknowledgements

This work was sponsored by the “World Premier International (WPI) Research Center Initiative for Atoms, Molecules and Materials”, Ministry of Education, Culture, Sports, Science, and Technology of Japan. We acknowledge financial support by the Japan Science and Technology Agency under the ERATO Isobe Degenerate  $\pi$ -Integration Project, the Mitsubishi Foundation, the European Union/JST FP7-NMP-2011-EU-Japan project LEMSUPER (contract no. NMP3-SL-2011-283214), and the UK Engineering and Physical Sciences Research Council (grant nos. EP/K027255 and EP/K027212). We thank the European Synchrotron Radiation Facility for access to synchrotron X-ray facilities, the Royal Society for a Newton International Fellowship (G.K.) and a Research Professorship (M.J.R.), A. N. Fitch for help with the synchrotron XRD experiments, H. Okazaki with the magnetic measurements, and K. Kamarás with the IR measurements.

### Additional information

The authors declare no competing financial interests. Supplementary information accompany this paper at [www.nature.com/naturechemistry](http://www.nature.com/naturechemistry). Reprints and permission information is available online at <http://www.nature.com/reprints>. Correspondence and requests for materials should be addressed to K.P.

### Author contributions

K.P. and M.J.R. conceived and designed the project. K.P. directed and coordinated the research. Y.T. and M.M. interpreted and discussed all results and carried out the final structural and magnetic work. H.T., N.T., T.K., Y.N. and R.A. carried out the calculations. A.Š. synthesised the materials. D.A. carried out EPR and G.K. vibrational spectroscopic work. A.J.C.B. and A.Š. carried out early structural and magnetic work. K.P. wrote the paper with input from all authors.

## Figure captions

**Figure 1 | Crystal structures of pristine phenanthrene and its caesium and dicaesium salts.** **a.** The phenanthrene molecule,  $C_{14}H_{10}$ . **b.** The herringbone structure of pristine phenanthrene (space group  $P2_1$ , lattice constants:  $a=8.472(4)$  Å,  $b=6.166(4)$  Å,  $c=9.467(5)$  Å,  $\beta=98.01(5)^\circ$  and  $V=489.7(5)$  Å<sup>3</sup> at 297 K)<sup>28</sup>. The dotted lines mark the slip-stacked 1D molecular columns along  $b$ —the interplanar angles between the mean plane of each molecule and that of its neighbours are  $58.21(7)^\circ$ . **c.** The crystal structure of orthorhombic  $Cs(C_{14}H_{10})$  is built by tubular assemblies of vertex-sharing triangularly-arranged trimers of  $(C_{14}H_{10})^{*-}$  radical anions (centre-to-centre connections depicted in green shading) that align along the  $c$  axis. Dotted lines go through the centres of the molecules, which define the spiral molecular tubes. The herringbone packing motif of pristine phenanthrene solid has been abandoned and  $Cs^+$  incorporation is accompanied by  $\sim 16\%$  volume expansion. **d.** Basal plane projection of the structure of  $Cs(C_{14}H_{10})$  emphasizing the parallel stacking of the individual quasi-one-dimensional molecular tubes perpendicular to the  $ab$  plane. Each tube (gold (blue) shading) is surrounded by four neighbours (blue (gold) shading) oriented at nearly right angles (alternately at  $87.670(8)^\circ$  and  $92.330(8)^\circ$ , respectively). The unit cell is depicted by dashed lines. **e.** Zig-zag chains of  $(C_{14}H_{10})^{*-}$  ions from neighbouring tubes running along the  $b$  axis. **f.** Perspective view down the  $c$  axis of the crystal structure of monoclinic  $Cs_2(C_{14}H_{10})$ . The unit cell is depicted by dashed lines. Herringbone packing is also abandoned and  $Cs^+$  incorporation is accompanied by  $\sim 27\%$  volume expansion. Dotted lines go through the centres of molecules with parallel ring orientation. The interplanar angles are  $72.3(6)^\circ$ . Key: grey, C; purple, Cs; orange, H.

**Figure 2 | Structural and vibrational characterisation of caesium phenanthrene salts.** **a.** Final observed (red circles) and calculated (blue solid line) synchrotron X-ray ( $\lambda=0.35420$  Å) powder diffraction profiles for the  $Cs(C_{14}H_{10})$  (**1**) sample at 30 K. **b.** Final observed (red circles) and calculated (blue solid line) X-ray ( $\lambda=1.54056$  Å, Cu  $K_{\alpha 1}$ ) powder diffraction profiles (after background subtraction) for the  $Cs_2(C_{14}H_{10})$  (**2**) sample at ambient temperature. The lower green solid lines in both panels show the difference profiles and the tick marks show the reflection positions. The insets in both panels show expanded views of the corresponding diffraction profiles at high Bragg angles. **c.** IR (top) and Raman ( $\lambda=532$  nm excitation, bottom) spectra of  $C_{14}H_{10}$  (black),  $Cs(C_{14}H_{10})$  (blue) and  $Cs_2(C_{14}H_{10})$  (green) at ambient temperature. Green arrows mark the shifts of two characteristic Raman peaks. The  $1349\text{-cm}^{-1}$  peak redshifts by 17 and  $7\text{ cm}^{-1}$  upon uptake of one and two electrons, respectively; the IR spectrum shows an identical shift (red arrows). The  $1439\text{-cm}^{-1}$  peak shows a linear redshift of  $\sim 42\text{ cm}^{-1}$ /elementary charge.

**Figure 3 | Evolution of magnetic properties upon reduction of phenanthrene.** **a.** Temperature dependence of the molar magnetic susceptibility,  $\chi$ , of **1** (blue circles) and **2** (green circles) measured in FC runs at 1 and 5 T, respectively.  $\chi(T)$  of **2** follows the Curie-Weiss law, yielding a temperature-independent term,  $\chi_0=1.21(9)\times 10^{-4}$  emu mol<sup>-1</sup>, a Curie constant,  $C=0.01065(5)$  emu K mol<sup>-1</sup> (corresponding to a spin concentration of 0.03 spin/molecule, ascribed to lattice defects), and a Weiss temperature,  $\Theta=-3.78(3)$  K. **b.** Temperature evolution of the X-band EPR spectra for  $Cs(C_{14}H_{10})$  powder (open circles). Solid red lines are fits of the data to a model of two overlapping components: the main broad one with a Lorentzian lineshape (blue line) dominates the spectra above  $\sim 15$  K, whereas the much narrower minority one ( $\Delta B_x=1.62(2)$  mT,  $\Delta B_y=\Delta B_z=0.47(2)$  mT, green line) has a lineshape characteristic of a small uniaxial  $g$ -factor anisotropy ( $g_{xx}=1.998(1)$  and  $g_{yy}=g_{zz}=2.001(1)$ ) and

prevails at the lowest temperatures where it solely accounts for the spectrum at 6 K. **c.** Temperature dependence of the intensity of the broad main component of the EPR spectra of Cs(C<sub>14</sub>H<sub>10</sub>) powder (filled brown squares). The maximum at  $T_{\max} \sim 42$  K coincides with that observed in  $\chi(T)$  by SQUID magnetometry (open blue circles). The intensity of the weak narrow EPR component (filled green squares) follows a Curie-like dependence (solid green line) with  $C=0.0177(2)$  emu K mol<sup>-1</sup> (corresponding to  $\sim 5\%$  of spins) and  $\Theta = -2(1)$  K. After subtraction of the intensity contribution of the Curie-like line from  $\chi(T)$  (open grey circles), the SQUID and EPR results coincide. Global fit of the data to a model of  $S=1/2$  Heisenberg antiferromagnetic alternating chain (solid red line) yields  $J/k_B=77.9(3)$  K,  $\alpha=0.687(5)$ , and  $C=0.301(1)$  emu K mol<sup>-1</sup> (consistent with the  $S=1/2$  state of the (C<sub>14</sub>H<sub>10</sub>)<sup>•+</sup> radical ions). As a consistency check, we show that the total EPR spin susceptibility calculated as the sum of the antiferromagnetic chain and Curie-like contributions (dashed purple line) tracks well the measured SQUID spin susceptibility,  $\chi(T)$ . *Inset.* Expanded view of the spin susceptibility at low temperatures. The solid blue line is a fit of the data up to 18 K to an exponential function,  $\chi(T) \propto \exp(-\Delta/T)$  with a spin-excitation gap,  $\Delta=30.7(7)$  K.

**Figure 4 | Electronic band structures of Cs(C<sub>14</sub>H<sub>10</sub>) and Cs<sub>2</sub>(C<sub>14</sub>H<sub>10</sub>).** **a.** Calculated density-of-states (left panel) and DFT-PBE band dispersions (right panel) of Cs(C<sub>14</sub>H<sub>10</sub>). The unit cell contains eight formula units and each molecule has two nearly-degenerate LUMO and LUMO+1 orbitals. Therefore there are sixteen bands in total. The energies are plotted along lines in the Brillouin zone connecting points  $\Gamma=(0,0,0)$ ,  $X=(1/2,0,0)$ ,  $S=(1/2,1/2,0)$ ,  $Y=(0,1/2,0)$ ,  $Z=(0,0,1/2)$ , and  $R=(1/2,1/2,1/2)$ . **b.** Calculated density-of-states (left panel) and DFT-PBE band dispersions (right panel) of Cs<sub>2</sub>(C<sub>14</sub>H<sub>10</sub>). The unit cell contains four formula units and each molecule has two nearly-degenerate LUMO and LUMO+1 orbitals. Therefore there are eight bands in total. The energies are plotted along lines in the Brillouin zone connecting points  $\Gamma=(0,0,0)$ ,  $C=(0,1/2,1/2)$ ,  $Z=(0,0,1/2)$ ,  $Y=(0,1/2,0)$ , and  $X=(1/2,0,0)$ . In both **a.** and **b.**, the weights of the LUMO- and (LUMO+1)-orbitals are depicted in blue and red, respectively and the zero of the energy is at the Fermi level.

**Figure 5 | First-principles calculations of the electronic and magnetic interactions in Cs(C<sub>14</sub>H<sub>10</sub>).** **a.** Alternating-exchange antiferromagnetic chain along the triangular lattice of the spin tubes aligned along the  $c$  axis with orange solid and dotted lines marking the strongest,  $J$  and second strongest,  $\alpha J$  interactions, respectively together with schematic representation of the non-frustrated up and down spin topology. **b.** Diagrammatic spin configuration on the fully-frustrated chains of corner-sharing triangular units ( $\Delta$ -chains) linking neighbouring tubes along the  $b$  axis. If the spin orientation of two anions is decided (blue and red arrows; the resulting singlet is shown as an orange oval), the remaining one (question mark) is left frustrated: it cannot decide with which of the two its spin should align antiparallel. The two distinct interchain couplings,  $J_{\text{inter}}$  and  $J'_{\text{inter}}$  are depicted as green dashed and pink dot-dashed lines, respectively. **c.** Microscopic magnetic model for Cs(C<sub>14</sub>H<sub>10</sub>). A staircase-like 3D interlinked arrangement arises by unequal-leg  $J$ - $\alpha J$  spiral tubes running along  $c$  that are coupled by two inequivalent couplings,  $J_{\text{inter}}$  and  $J'_{\text{inter}}$  to form frustrated  $\Delta$ -chains running along  $b$ . The same colouring scheme is used as above. An example of the exchange pathway along the spin tubes is marked in thicker orange solid and dotted lines.

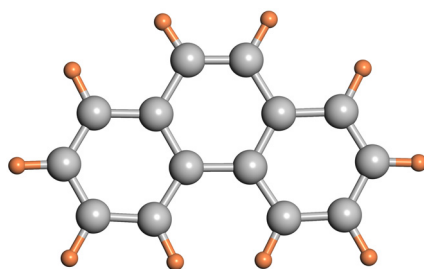


Fig. 1a

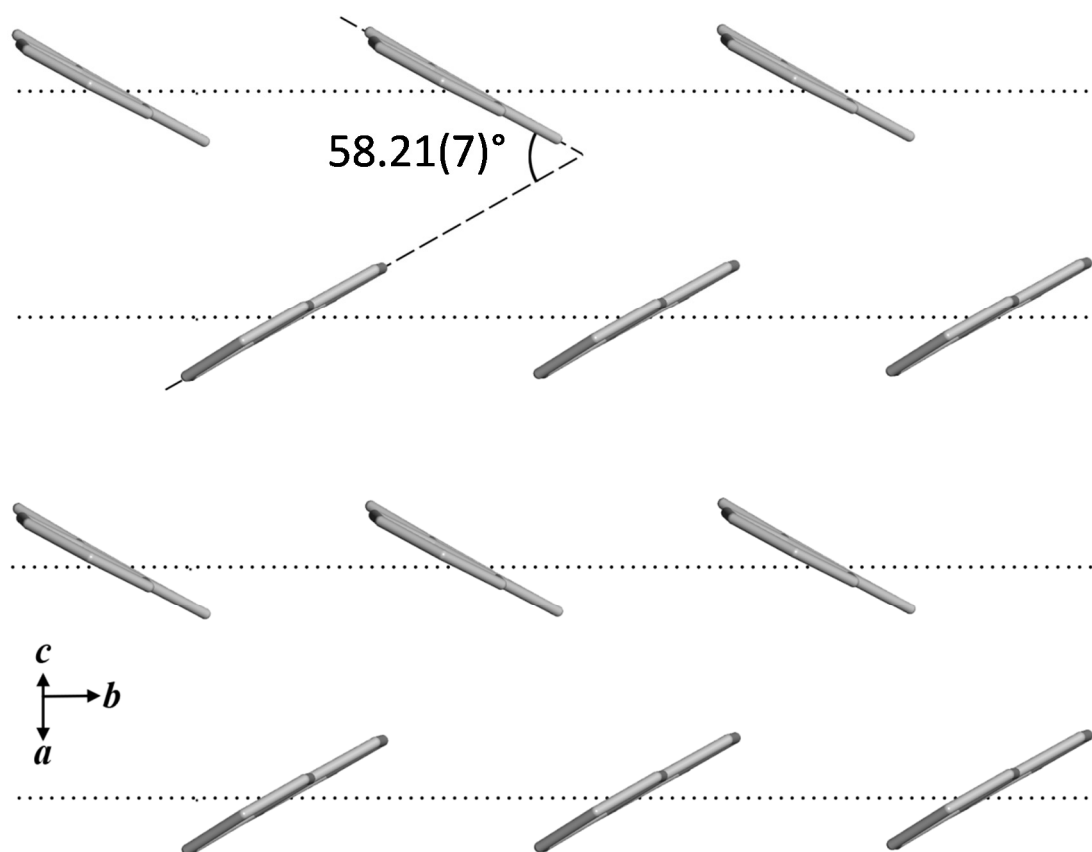


Fig. 1b

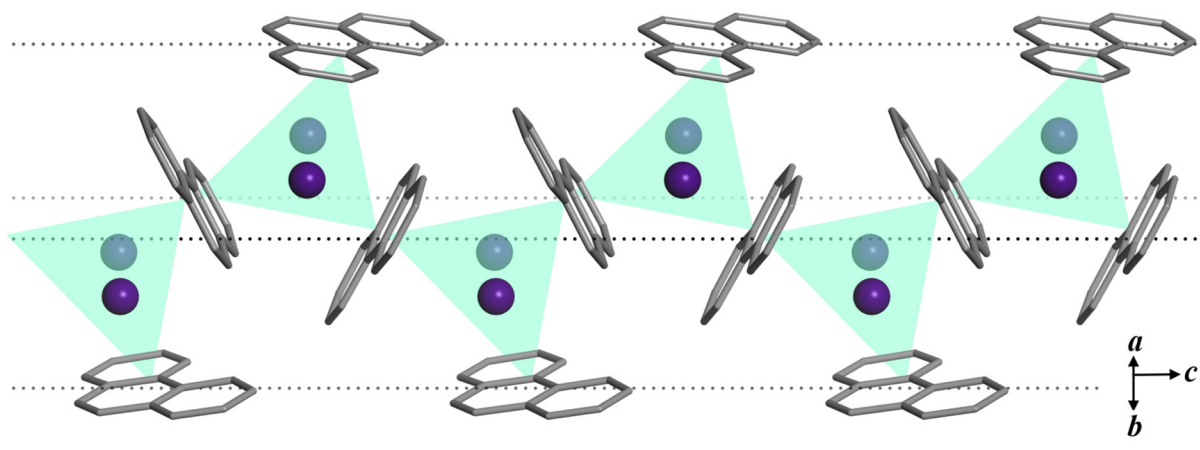


Fig. 1c

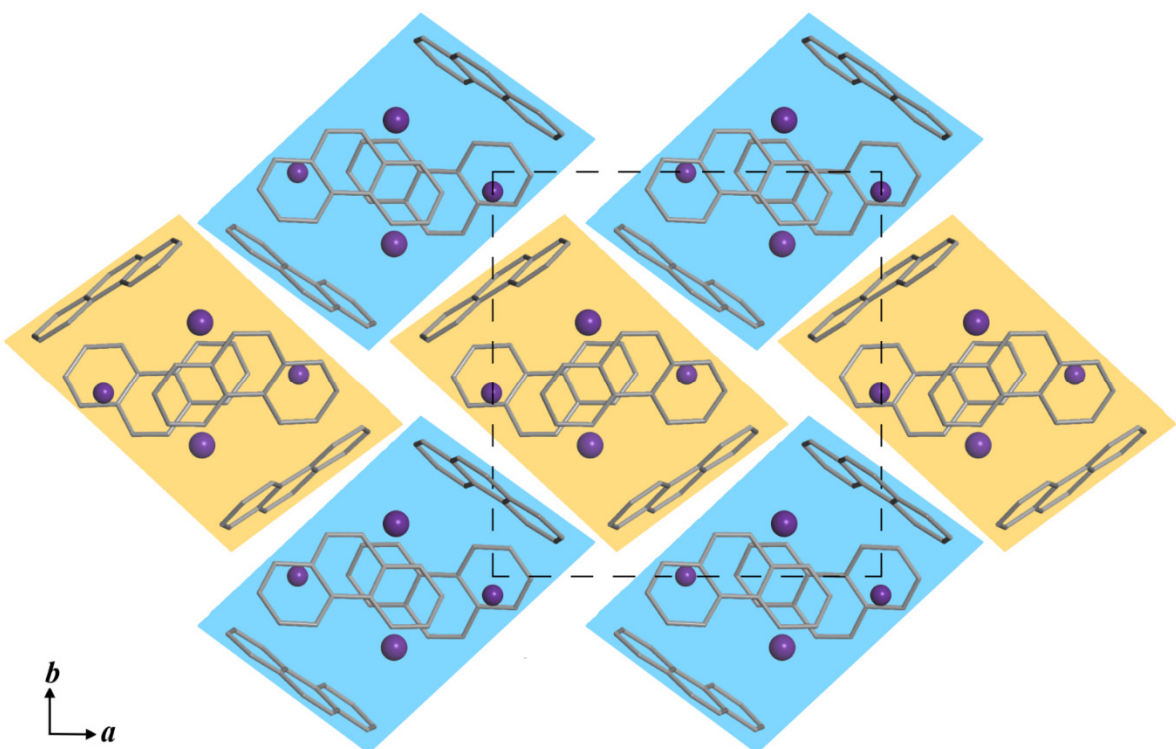


Fig. 1d

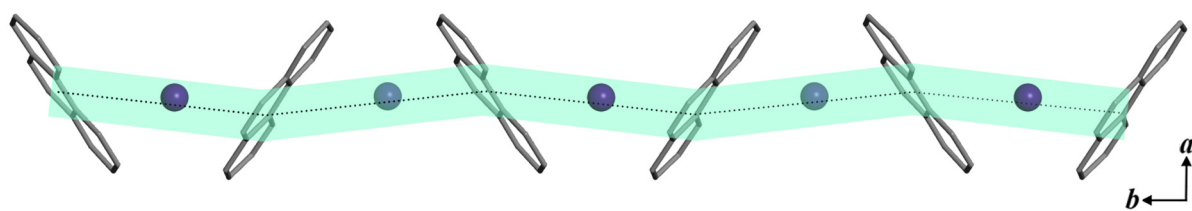


Fig. 1e

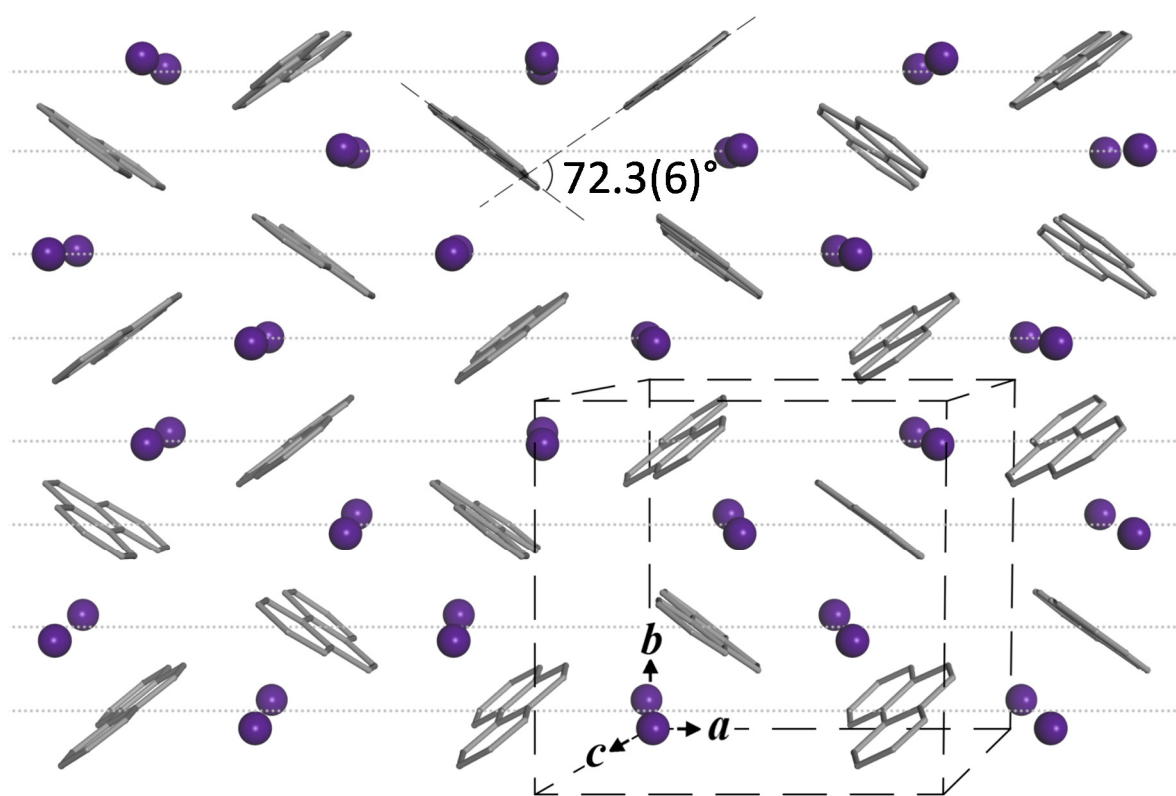


Fig. 1f



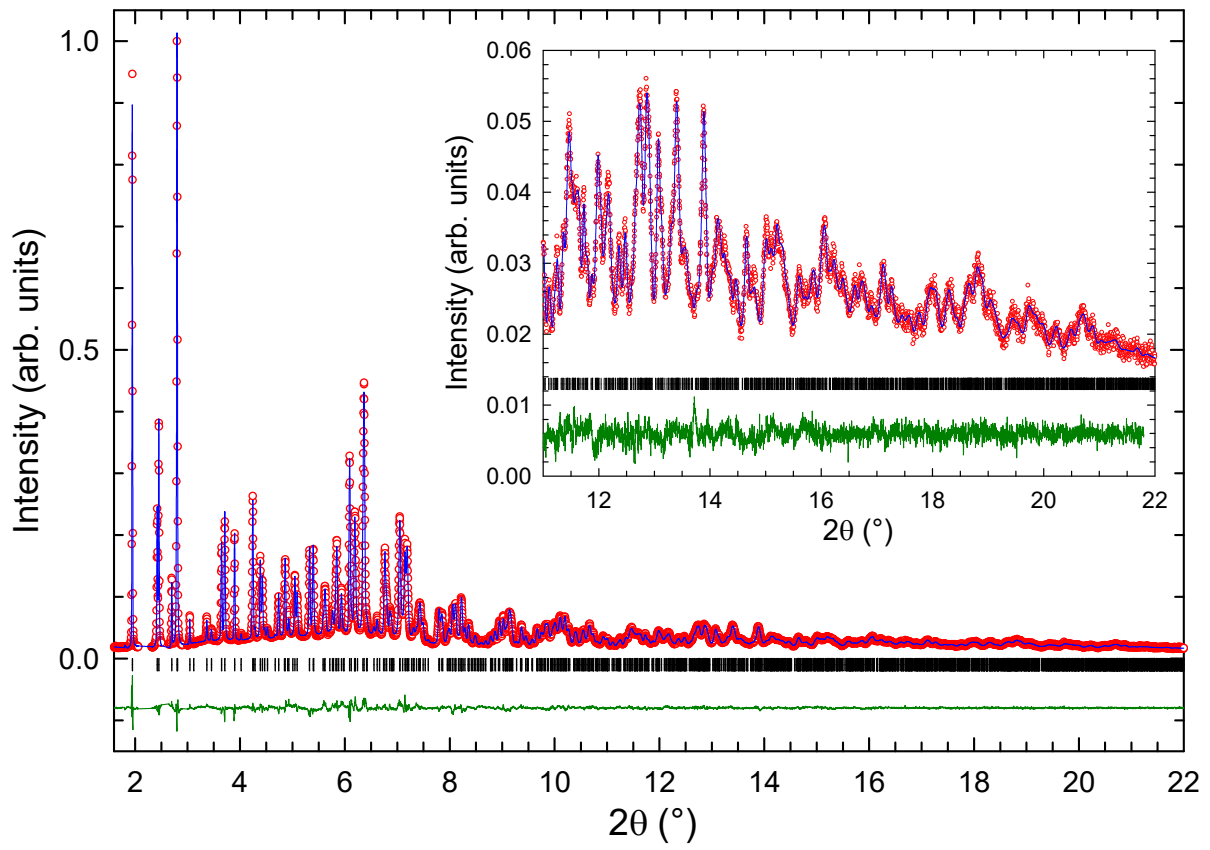


Fig. 2a

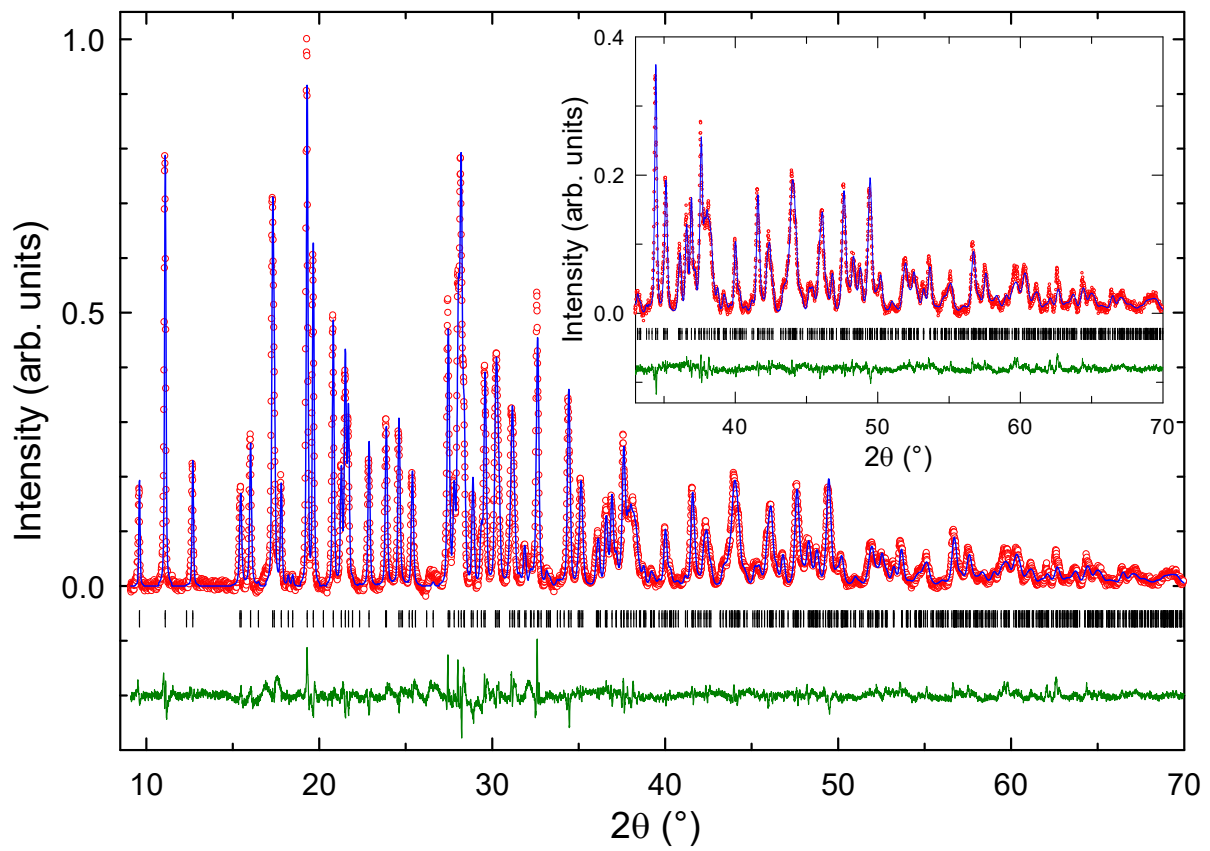


Fig. 2b

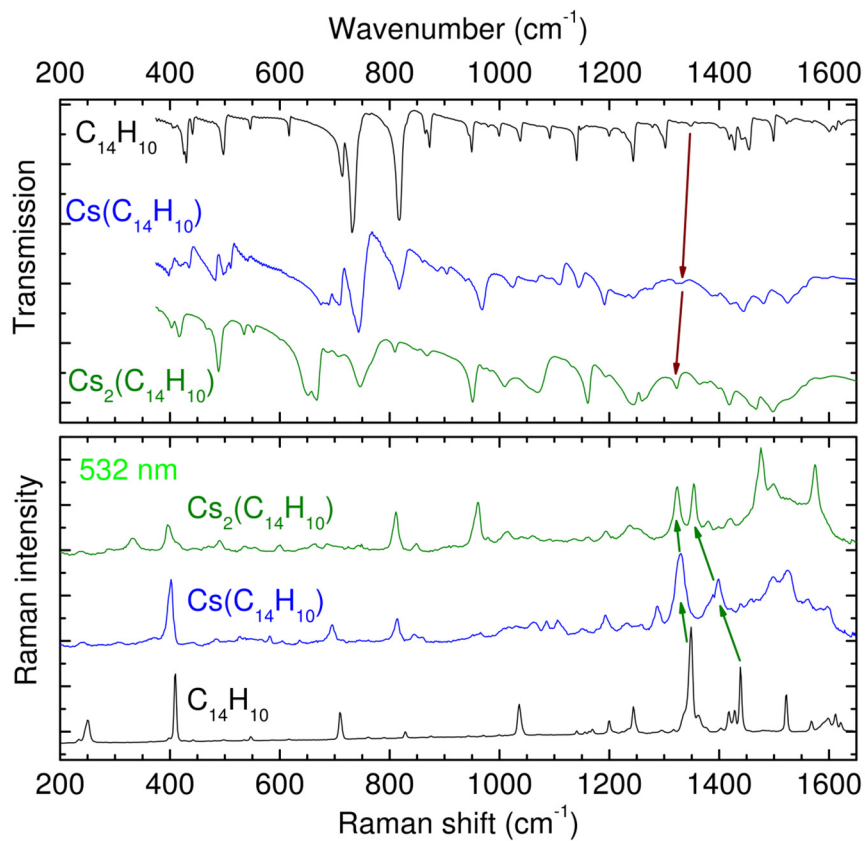


Fig. 2c

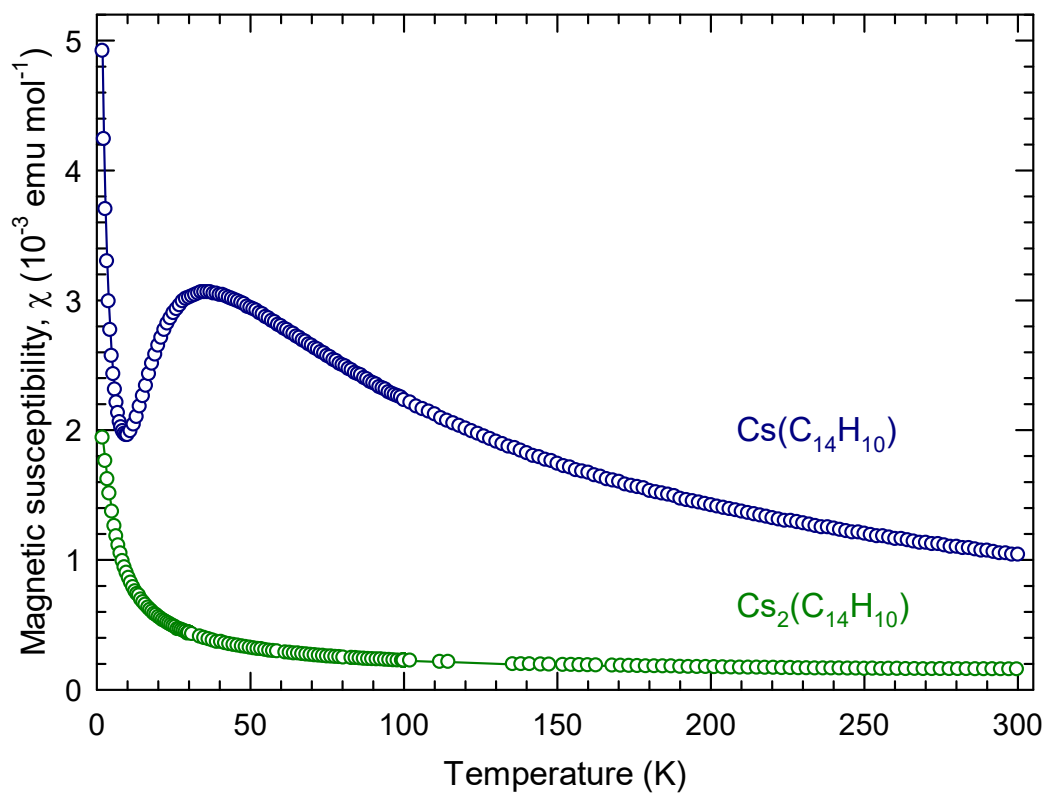


Fig. 3a

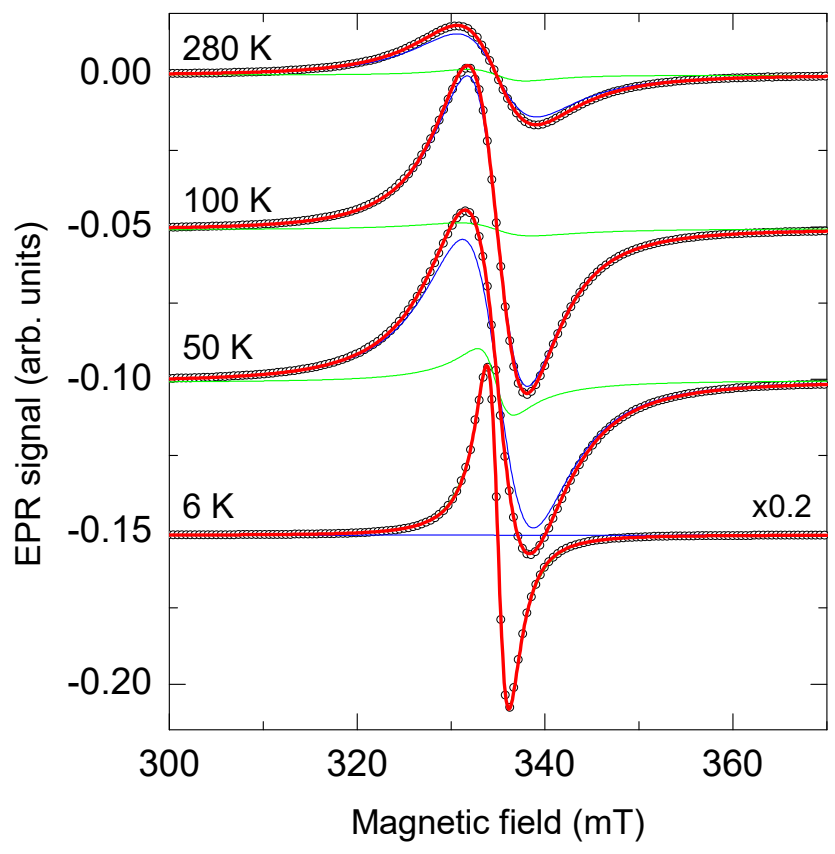


Fig. 3b

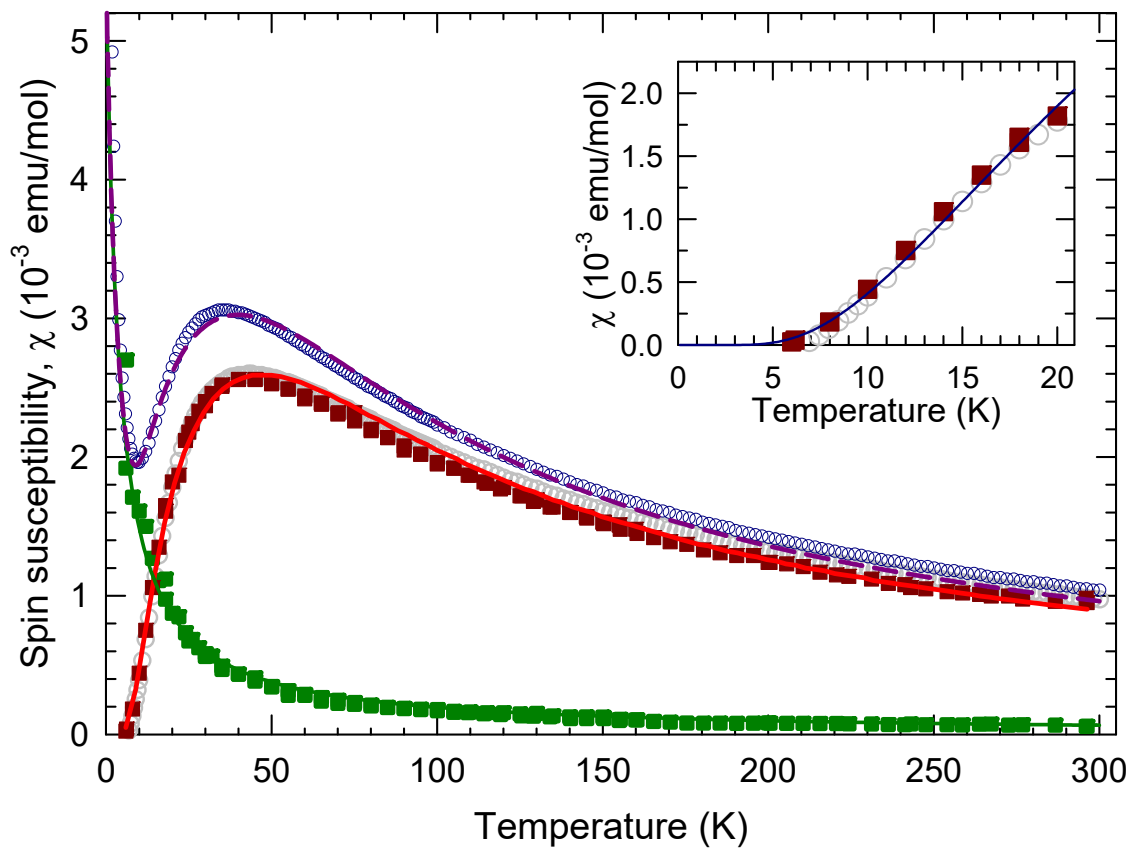


Fig. 3c

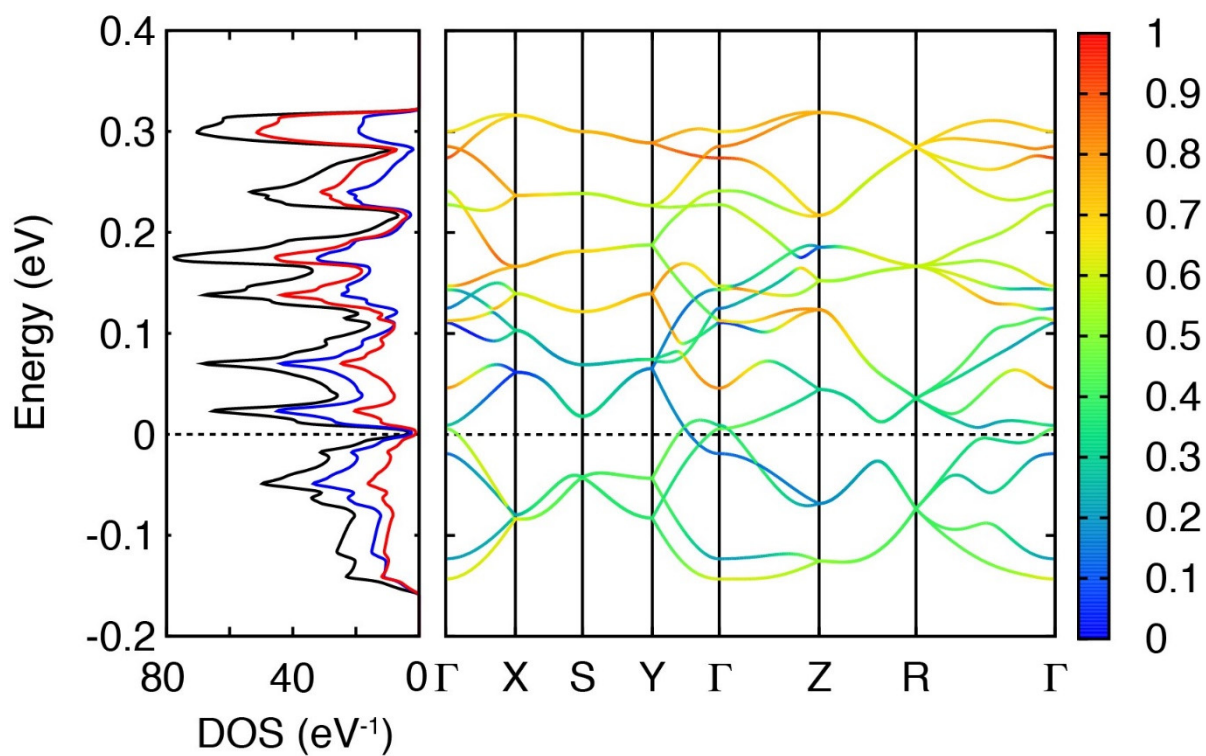


Fig. 4a

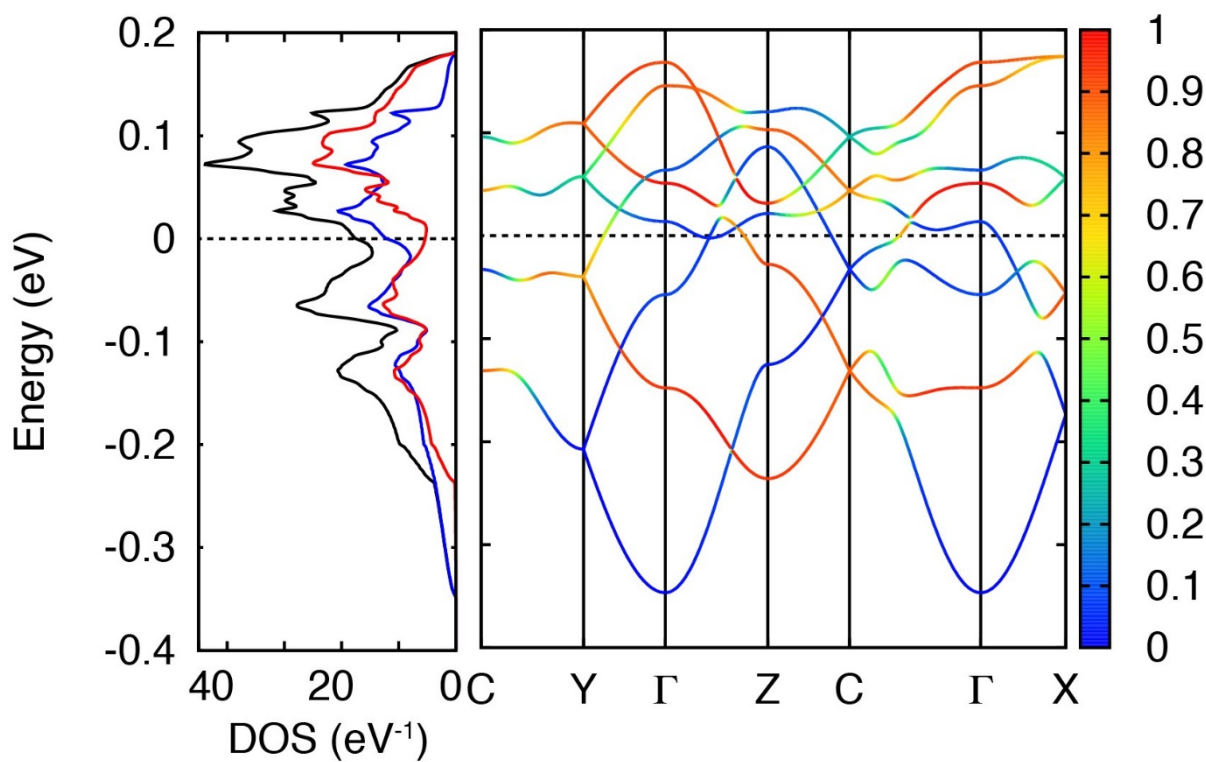


Fig. 4b

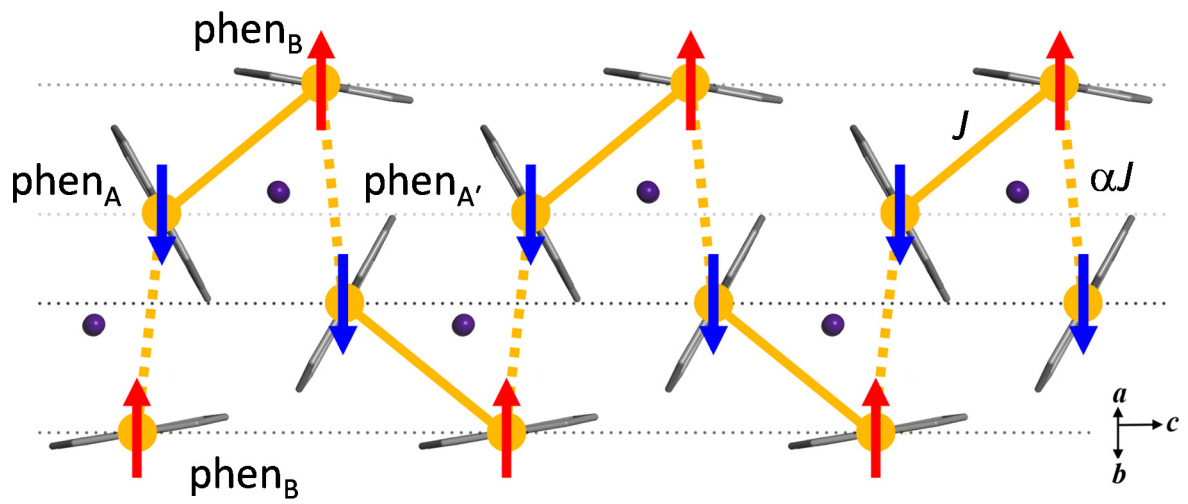


Fig. 5a

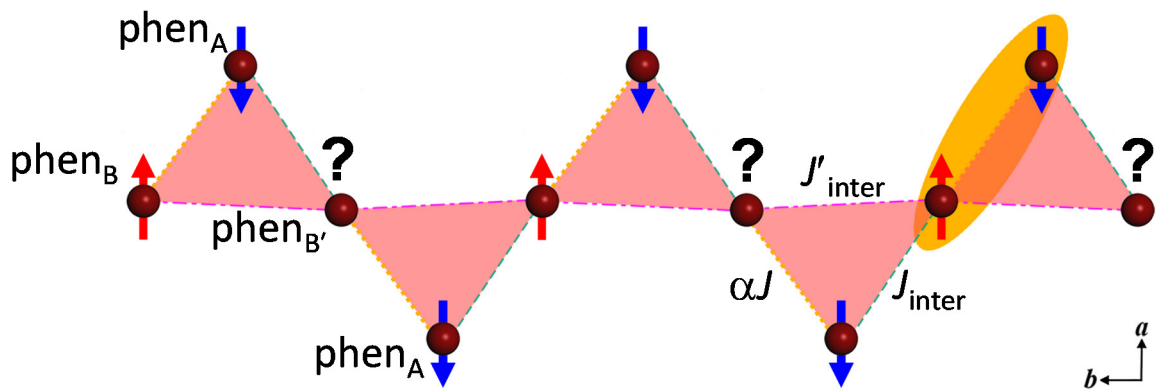


Fig. 5b

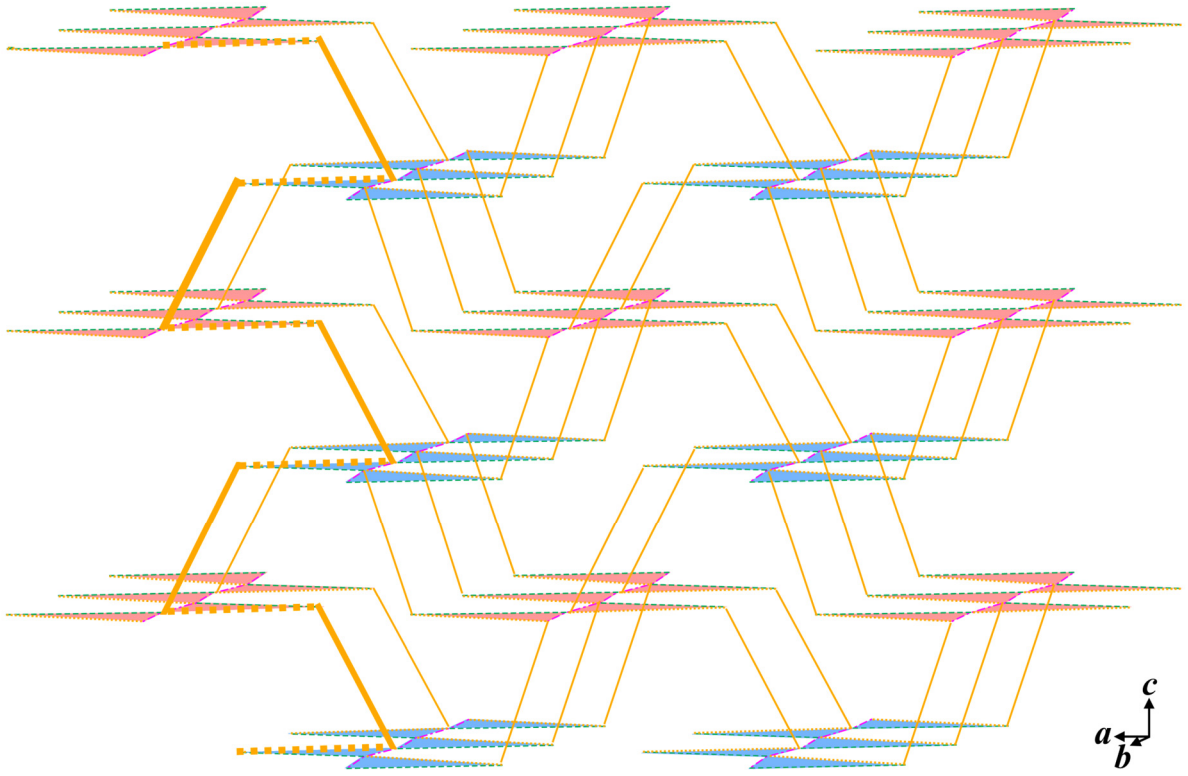


Fig. 5c